

Leonie Schicketanz*, Laura Anna Unger, Jorge Sánchez, Olaf Dössel, and Axel Loewe

Separating atrial near fields and atrial far fields in simulated intra-atrial electrograms

Abstract: The detailed characterization of complex forms of atrial flutter relies on the correct interpretation of intra-atrial electrograms. For this, the near field components, which represent the local electrical activity, are decisive. However, far field components arising from distant electrical sources in the atria can obscure the diagnosis. We developed a method to separate and characterize atrial near field and atrial far field components from bipolar intra-atrial electrograms. First, a set of bipolar electrograms was created by simulating different propagation scenarios representing common clinical depolarization patterns. Second, near and far fields were detected as active segments using a non-linear energy operator-based approach. Third, the maximum slope and the spectral power were extracted as features for all active segments. Active segments were grouped accounting for both the timing and the location of their occurrence. In a last step, the active segments were classified in near and far fields by comparing their feature values to a threshold. All active segments were detected correctly. On average, near fields showed 15.1x larger maximum slopes and 40.4x larger spectral powers above 100 Hz than far fields. For 135 active segments detected in 72 bipolar electrograms, 5.2% and 6.7% were misclassified using the maximum slope and the spectral power, respectively. All active segments were classified correctly if only one near field segment was assumed to occur per electrogram. The separation of atrial near and atrial far fields was successfully developed and applied to in silico electrograms. These investigations provide a promising basis for a future clinical study to ultimately facilitate the precise clinical diagnosis of atrial flutter.

Keywords: atrial flutter, atrial near field, atrial far field, cardiac modeling, electrogram

<https://doi.org/10.1515/cdbme-2021-2045>

*Corresponding author: **Leonie Schicketanz:** Institute of Biomedical Engineering, Karlsruhe Institute of Technology (KIT), Fritz-Haber-Weg 1, 76131 Karlsruhe, Germany, e-mail: publications@ibt.kit.edu

Laura Anna Unger, Jorge Sánchez, Olaf Dössel, Axel Loewe
Institute of Biomedical Engineering, Karlsruhe Institute of Technology (KIT), Karlsruhe, Germany

1 Introduction

Atrial flutter (AFlut) is a common atrial tachycardia, which is not life-threatening but can cause severe comorbidities such as cerebral stroke. For diagnosis, physicians interpret intra-atrial electrograms (EGMs) in minimal-invasive electrophysiological studies to identify local electrical activity, so-called near fields. However, far fields complicate the interpretation of EGMs since they are caused by the sum of distant electrical depolarization. Atrial far fields may occur due to broad activation waves passing a distant part of the atrium or an excitation spread at the opposite side of a line of block.

So far, methods have only been developed to eliminate ventricular far fields [1]. Thus, methods to identify atrial far fields are still missing. In this study, we explore the extent to which atrial near fields and atrial far fields can be distinguished. Towards this goal, an algorithm was developed to detect, characterize, and classify both components in simulated bipolar electrograms (B-EGMs).

2 Methods

2.1 Simulation setup

Figure 1 shows the simulation setups representing common clinical scenarios established within a square patch of tissue. Lines of block guided the spread of depolarization and provoked far field signals. The bidomain model was used for the simulations using openCARP [2].

The tissue patch had dimensions of $30 \times 30 \times 2.1$ mm [3] and was surrounded by a $34 \times 34 \times 10$ mm bath. The transmural lines of block were 0.3 mm wide, which proved sufficient to block an excitation wave. The electrode grid was based on the Advisor™ HD Grid Mapping catheter, Sensor Enabled™ (Abbott, Chicago, IL, USA) and comprised 16 equidistant cuboid electrodes with an edge length of 0.9 mm. The overall mesh resolution was 0.3 mm.

The following isotropic extracellular conductivities were implemented: 0.7 S/m for the bath [4], 10^6 S/m for the electrodes [5], and 0.55 S/m for the line of block, which

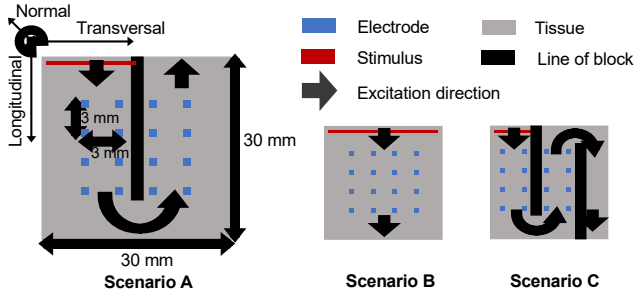


Figure 1: Simulation setups including dimensions and fiber orientation (visualized as axes of coordinates in longitudinal, transversal, and normal direction).

represented a myocardial lesion without any viable cells [6]. For the tissue patch simulation, the Courtemanche et al. [7] model was used. The ionic channels maximum conductances were modified to represent remodeling induced by atrial fibrillation (AFib) [8]. For the conduction velocity (CV), 43.39 cm/s and 100 cm/s were chosen. The former value represents a CV commonly found in tissue remodeled by AFib [9], while the latter was considered physiological [10]. For AFib-induced anisotropic conduction, the following ratios were selected for the intracellular conductivities: 2:1 as the ratio between longitudinal and transversal conduction and 10:1 as the ratio between longitudinal and normal conduction [9,11,12].

The tissue was stimulated with a transmembrane current of strength $500 \mu\text{A}/\text{cm}^2$ for a duration of 2 ms. The sampling frequency f_s of the output data was 2 kHz. The temporal course of the extracellular potentials was extracted and averaged for all elements within an electrode, yielding unipolar electrograms (U-EGMs). U-EGMs of adjacent electrodes in line with the main direction of excitation propagation were subtracted to obtain B-EGMs.

2.2 Active segment detection

Both near and far fields cause activity in the B-EGM. The active segments, thus near and far fields, were detected based on the non-linear energy operator (NLEO) [13]. As a threshold upon which high energy signal parts were classified as active, the following values were applied to the standard deviation of the NLEO signal: 0.35 for signals based on a CV of 43.39 cm/s and 3.5 for a CV of 100 cm/s. However, since far fields contained less energy than near fields due to weaker amplitudes and flatter curves, not all active components could be detected at once with this method. Thus, the algorithm was enhanced by iteratively detecting and eliminating active segments. In this way, after components with the highest energy were extracted, components with smaller energy, were now detectable. This was repeated at most 5 times or until the maximum signal energy fell below $1.9 \times 10^{-5} \text{ mV}^2$ for signals

based on a CV of 43.39 cm/s and $1.1 \times 10^{-4} \text{ mV}^2$ for a CV of 100 cm/s. To eliminate the detected active segment, the segment was replaced with either a linear interpolation or a Gaussian bell converging to the baseline at 0 mV. The Gaussian approximation method aimed at resembling far fields that were close to a near field. It was applied if the signal at the border exceeded 0.15 of the absolute amplitude of the first detected segment, and if a maximum was detected adjacent to the first detected active segment. The corresponding window width to identify possible maxima was chosen as the length of the detected active segment. Otherwise, the active segment border was linearly interpolated.

2.3 Feature extraction

The maximum slope and the spectral power were chosen to characterize an active segment. The maximum slope was equal to the maximum value of the differentiated active segment. The spectral power was calculated by applying the short-time Fourier transform to each B-EGM, generating a power spectral density (PSD). The width of the window function was set to 20 ms based on the average duration of an active segment. The spectral power for an active segment was then estimated by trapezoidal integration:

$$P \approx \frac{\Delta f}{2} \sum_{n=f_\alpha}^{\frac{f_s}{2}} (\text{PSD}(f_n) + \text{PSD}(f_{n+1}))$$

As near and far fields were assumed to differ in their high frequency content, only the frequencies above $f_\alpha = 100 \text{ Hz}$ were considered. The spacing Δf between the equidistant points f_n was 7.8125 Hz. For this method, a correct active segment detection was assumed as input.

2.4 Spatio-temporal classification of active segments

The active segments identified in B-EGMs of one scenario were grouped if the active time intervals of neighboring electrodes overlapped by at least 60%. These groups were called ‘matched active segment groups’ (MASGs) and contained active segments that shared the same point in time but did not originate from the same location. Due to the spatio-temporal relationship in a MASG, the corresponding active segments were assumed to stem from the same electrical activity. Thus, feature values of active segments in one MASG were presumably in the same order of magnitude. For this reason, only the active segments that were part of a MASG were considered for the classification of active segments into near and far fields. The corresponding feature values were

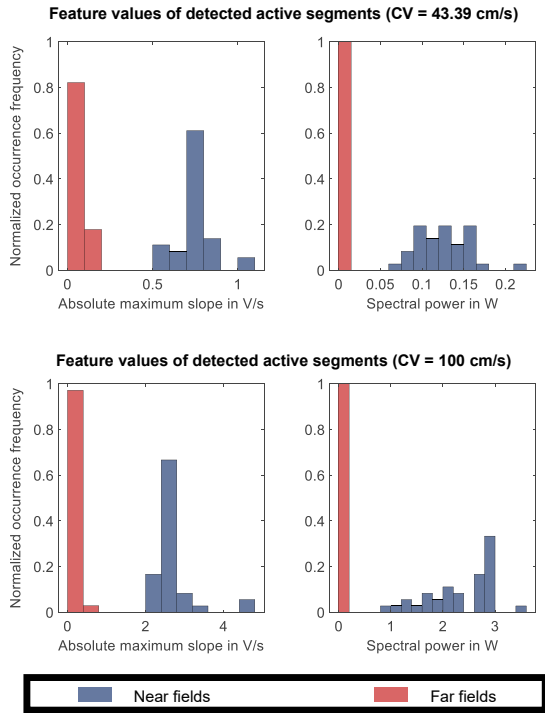


Figure 2: Normalized occurrence frequency of the maximum slopes and the spectral powers of the active segments detected in the B-EGMs of scenarios A – C.

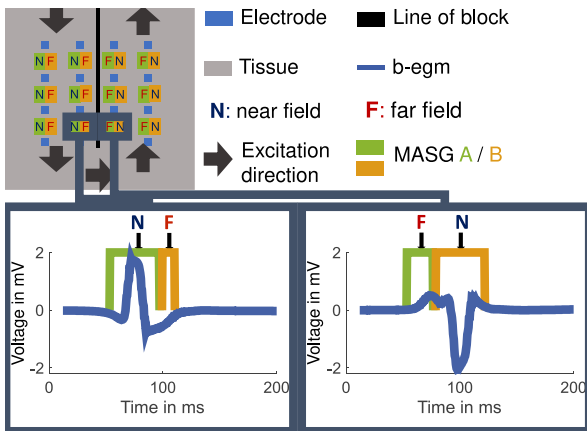


Figure 3: Schematic showing both MASGs of scenario A and illustrating the spatio-temporal relationship between near and far fields. The colored squares represent the B-EGMs of the 4 x 4 electrode grid in line with the main propagation direction.

compared to a threshold which was the product of a factor α and the maximum feature value of the MASG. Exceeding the threshold indicated a near field, otherwise a far field. α was set to 0.3 for the slope feature and to 0.15 for the power feature. Additionally, if more than one near field was detected in a B-EGM, only the active segment with the highest maximal slope was considered a near field, labelling the others as far fields.

3 Results

For all B-EGMs, the active segments were detected correctly. Concerning the feature extraction, Figure 2 shows a visible gap between near and far fields. On average, near fields showed 15.1 times larger maximum slopes and 40.4 times larger spectral power than far fields. Figure 3 exemplarily demonstrates the successful matching of active segments based on the time and location of their occurrence as observed for all scenarios. Furthermore, Figure 3 indicates that a near field on one side of the line of block coincides with a far field on the opposite side. For scenarios A and B, all segments were classified correctly for both feature comparison procedures. In scenario C, far fields recorded in B-EGMs next to the right line of block were misclassified. The error rate was the number of falsely classified active segments over the total number of segments detected in all B-EGMs with 6.7 % for the power feature comparison and 5.2 % for the slope feature comparison. All segments were classified correctly if only one near field was assumed to occur per B-EGM.

4 Discussion

For the active segment detection as well as the threshold-dependent segment classification, parameters were tuned using the presented in silico EGMs. For this data, the method was robust since the parameters were based on a known distance to the source, CV, and main propagation direction of the excitation wave. However, in clinical setups this is not the case. The following aspects should therefore be considered in future work: Increasing distance to the electrical source leads to decreased and flattened deflections of active signal components as the recorded field intensity of the electrical activity decreases. This occurs either by lifting the electrodes from the tissue or by moving them away from a distant source. Creating MASGs partially solves this problem as in one group only active segments are considered that occur at the same time and thus were likely to have deflections of comparable magnitude. However, feature comparison through thresholding is challenging when near and far field morphologies and thus feature values become more alike with increased distance to the tissue. Additionally, broad wavefronts with large excited tissue areas may also provoke far fields with feature values in the order of magnitude of near fields. In rare cases, if near fields have small amplitudes in relation to far fields or do not exist, this can lead to misclassified active segments. When using MASGs for classification, this condition is negligible.

Another limitation are different CVs because e.g., increasing CV leads to sharper deflections due to faster propagating excitation waves. Different CVs change the maximum slope and the spectral power of the active segments and thus require adaptive parameters. Here, estimating the CV beforehand would allow adjusting the algorithm accordingly.

Furthermore, this work was simplified by expecting the B-EGMs to align with the excitation direction. Otherwise, the active segments would change their morphology. To ensure the correct B-EGM alignment, omnipolar EGMs (O-EGMs) [14] could be used as they adapt automatically to the direction of propagation of the near field. Far fields are not crucial for the calculation of O-EMGs, even though the morphology of far fields is also dependent on the orientation of its wave front. Yet, this aspect will not affect the correct classification of far fields as long as the far field features are correctly interpreted.

Also, we simulated only one position of a static electrode grid instead of moving the catheter across the tissue. If far fields were recorded with corresponding near field origin outside the covered area, the classification failed. In scenario C, this error occurred for those B-EGMs close to the right line of block. Here, the corresponding electrodes recorded far fields which resulted from the excitation wave passing on the right side of the line of block. Since no electrode recorded the according near field, the threshold calculation for the MASG was only based on far fields. In this work, this was prevented by allowing only one near field per B-EGM. Yet, moving the electrode grid for sequential mapping as common clinical practice should avoid this circumstance altogether.

Additionally, U-EGMs should be considered in future work due to their independence from propagation direction even though they are prone to noise and are therefore not commonly used in clinical studies.

In summary, we successfully developed and applied a feature-based, spatio-temporal separation method to in silico EGMs building a promising basis for facilitating the precise clinical diagnosis of AFlut. Further studies will have to investigate the robustness of our proposed method in a clinical setup.

Author Statement

We gratefully acknowledge financial support by the Deutsche Forschungsgemeinschaft (DFG, German Research Foundation) – Project-ID 394433254 (DO 637/23-1). No conflict of interest.

References

- [1] D. Frisch, T. Oesterlein, L. Unger, et al. Mapping and Removing the Ventricular Far Field Component in Unipolar Atrial Electrograms. *IEEE Transactions on Biomedical Engineering*, vol. 67, no. 10, pp. 2905-2915, 2020.
- [2] G. Plank, A. Loewe, A. Neic, et al. The openCARP Simulation Environment for Cardiac Electrophysiology. *BioRxiv*, 2021.
- [3] S. Rossi, S. Gaeta, B. E. Griffith, et al. Muscle thickness and curvature influence atrial conduction velocities. *Frontiers in Physiology*, vol. 9, p. 1344, 2018.
- [4] S. Gabriel, R. W. Lau, and C. Gabriel. The dielectric properties of biological tissues: III. parametric models for the dielectric spectrum of tissues. *Physics in Medicine and Biology*, vol. 41, no. 11, pp. 2271–2293, nov 1996.
- [5] M. Keller. Formation of intracardiac electrograms under physiological and pathological conditions. PhD thesis, Karlsruhe Institute of Technology, 2014.
- [6] J. Greiner, A. C. Sankarankutty, G. Seemann, et al. Confocal microscopy-based estimation of parameters for computational modeling of electrical conduction in the normal and infarcted heart. *Frontiers in Physiology*, vol. 9, p. 239, 2018.
- [7] M. Courtemanche, R. J. Ramirez, and S. Nattel. Ionic mechanisms underlying human atrial action potential properties: insights from a mathematical model. *Am J Physiol*, vol. 275, no. 1 Pt 2, pp. 1522–1539, 1998.
- [8] A. Loewe, M. Wilhelms, O. Dössel, et al. Influence of chronic atrial fibrillation induced remodeling in a computational electrophysiological model. *Biomedizinische Technik*, vol. 59, pp. 929–932, 2014.
- [9] S. Zahid, H. Cochet, P. M. Boyle, et al. Patient-derived models link re-entrant driver localization in atrial fibrillation to fibrosis spatial pattern. *Cardiovascular Research*, vol. 110, no. 3, pp. 443–454, 04 2016.
- [10] O. Dössel, M. Krueger, F. Weber, et al. Computational modeling of the human atrial anatomy and electrophysiology. *Medical & Biological Engineering & Computing*, vol. 50, pp. 773–99, 06 2012.
- [11] A. Ferrer, R. Sebastián, D. Sánchez-Quintana, et al. Detailed anatomical and electrophysiological models of human atria and torso for the simulation of atrial activation. *PLOS ONE*, vol. 10, no. 11, p. e0141573, 2015.
- [12] M. A. Colman, O. V. Aslanidi, S. Kharache, et al. Proarrhythmogenic effects of atrial fibrillation-induced electrical remodelling: insights from the three-dimensional virtual human atria. *The Journal of Physiology*, vol. 591, no. 17, pp. 4249–4272, 2013.
- [13] M. P. Nguyen, C. Schilling, and O. Dössel. A new approach for automated location of active segments in intracardiac electrograms. *World Congress on Medical Physics and Biomedical Engineering*, September 7 - 12, 2009.
- [14] C. Deno, R. Balachandran, D. Morgan, et al., "Orientation independent catheter-based characterization of myocardial activation," *IEEE Transactions on Biomedical Engineering*, vol. 64, p 1, 07 2016